Research Article | Vol. 26, No. 19 | 17 Sep 2018 | OPTICS EXPRESS 25211
Optics EXPRESS

Holographic optical trapping Raman micro-spectroscopy for non-invasive measurement and manipulation of live cells

FARIS SINJAB,[1] DENNIS AWUAH,[2] GRAHAM GIBSON,[3] MILES PADGETT,[3] AMIR M. GHAEMMAGHAMI,[2] AND IOAN NOTINGHER[1]

[1]*School of Physics and Astronomy, University of Nottingham, University Park, NG7 2RD, UK*
[2]*Division of Immunology, School of Life Sciences, University of Nottingham, University Park, Nottingham, NG7 2RD, UK*
[3]*School of Physics and Astronomy, University of Glasgow, Kelvin Building, Glasgow G12 8QQ, UK*
[*]*ioan.notingher@nottingham.ac.uk*

Abstract: We present a new approach for combining holographic optical tweezers with confocal Raman spectroscopy. Multiple laser foci, generated using a liquid-crystal spatial light modulator, are individually used for both optical trapping and excitation of spontaneous Raman spectroscopy from trapped objects. Raman scattering from each laser focus is spatially filtered using reflective apertures on a digital micro-mirror device, which can be reconfigured with flexible patterns at video rate. We discuss operation of the instrument, and performance and viability considerations for biological measurements. We then demonstrate the capability of the instrument for fast, flexible, and interactive manipulation with molecular measurement of interacting live cell systems.

1. Introduction

Raman micro-spectroscopy (RMS) is a sensitive label-free analytical technique which is well suited to biomolecular measurement with high chemical specificity and diffraction-limited spatial resolution [1, 2]. Within the scope of cell biology, RMS has been applied to the study of a wide range of species, from single bacteria [3, 4], to fungal [5] and animal cells [6–8]. RMS has also been applied to the study of cell systems relevant to medicine, including immunology [9, 10], parasitology [11, 12], stem cell biology [13, 14], and cancer cell biology [15, 16]. RMS measurements usually involve tightly focusing a laser beam at a point on a sample, which excites spontaneous Raman scattering from the vibrational modes of the molecules in this region.

A suitable technique for controlling live cells is optical trapping/tweezing [17, 18], which has been demonstrated for a variety of applications across the life sciences [19, 20]. Modern holographic optical trapping (HOT) instruments are capable of generating many simultaneous trapping beams using liquid-crystal spatial light modulators (LC-SLM), which allow interactive control in real-time [21].

Optical trapping is a somewhat natural partner for RMS of single cells, as both techniques share many of the same requirements, such as the use of near-IR wavelengths to avoid absorption-induced damage, and improved performance with higher numerical aperture microscope objectives. Using a single focused laser beam, optical trapping has been combined with Raman spectroscopy for many biological applications, from the identification of bacterial spores to Raman activated cell sorting [4, 15, 16, 22–30].

Single-beam optical trapping is compatible with the instrumentation used for RMS which typically involves a confocal pinhole and/or a narrow spectrometer entrance slit to facilitate high spectral resolution. However with the multi-point HOT approach, a single pinhole and/or slit is not suitable as the Raman scattering from most positions would be prevented from reaching

#334828 https://doi.org/10.1364/OE.26.025211
Journal © 2018 Received 13 Jun 2018; revised 20 Jul 2018; accepted 20 Jul 2018; published 12 Sep 2018

Optics EXPRESS

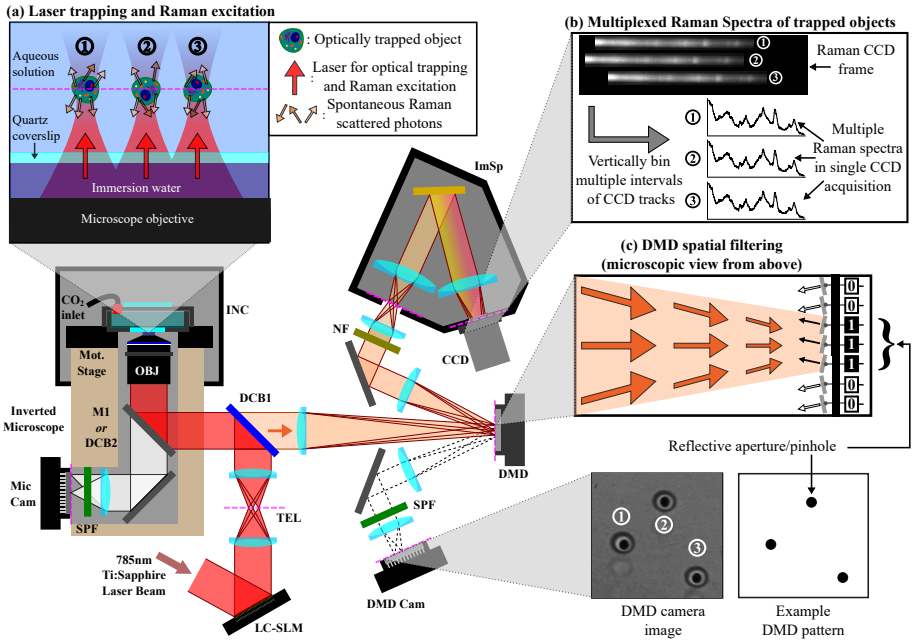

Fig. 1. HOT-RMS instrument. (a) Multiple laser foci are used to trap and excite Raman scattering from microscopic cells/particles. (b) Raman spectra from each trap can be read-out simultaneously at the CCD spectrograph, after spatial filtering at a DMD with reflective confocal pinhole patterns shown in (c). Glossary: LC-SLM: liquid-crystal spatial light modulator, INC: microscope incubator enclosure, TEL: $4f$ telescope relay, DCB: dichroic beamsplitter, OBJ: microscope objective, DMD: digital micro-mirror device, ImSp: imaging spectrometer, DMD Cam: CMOS inspection camera for DMD, SPF: short-pass filter, NF: notch filter, M: near infra-red mirror, Mic Cam: microscope camera. Dashed pink lines represent planes perpendicular to the optical axis which are sample-conjugate. Dashed black lines show rays reflected from the DMD plane away from the spectrometer direction.

the detector. Several approaches towards reconciling this problem have been proposed, such as using a rapidly scanned laser beam dwelling at multiple locations for time-shared multi-point measurement with a matched mirror to align sampling points into a spectrometer [29], power-shared excitation with an LC-SLM using a fixed array of electronically controlled pinholes [31] or imaging directly onto a detector for small highly scattering objects [32].

In order to fully utilize the flexibile laser-trap generation of the LC-SLM used for HOT in RMS, it is desirable to have a similarly rapid and flexible tool for producing an array of matched confocal pinholes. One method from fluorescence microscopy involves the use of a programmable digital micro-mirror device (DMD), which functions as a binary-choice reflective-mode SLM by directing incident light into one of two directions. The use of a DMD has been demonstrated both for confocal [33] and wide-field [34] fluorescence microscopy. Using this approach, reflective pinholes can also be generated to collect the Raman scattering from sampling positions generated by an LC-SLM [35].

Here, we describe a video-rate HOT-RMS instrument with detection using reflective pinholes on a DMD. This instrument can manipulate and simultaneously measure Raman spectra from several optically trapped objects. We demonstrate the capability and limits of the instrument for measuring RMS spectra from moving trapped polymer beads, as well as various power considerations for measurements of multiple trapped live cells. Finally we demonstrate an example of multi-cellular interactions involving HOT control and RMS readout involving the

Optics EXPRESS

formation of an immunological synapse between T cells and a dendritic cell (DC).

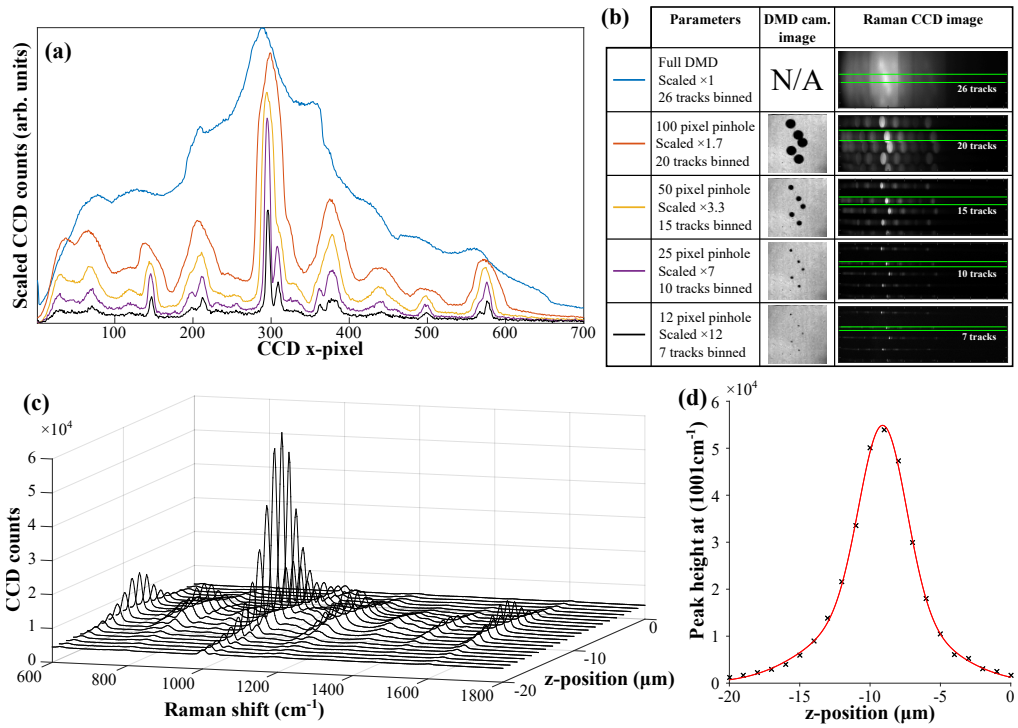

Fig. 2. Optimization of HOT-RMS signal collection. (a) RMS spectra acquired from bulk polystyrene for different DMD pinhole configurations with parameters outlined in (b). (c) RMS spectra acquired for a single 3 μm polystyrene microparticle manipulated axially through the objective focus (z-position) using RedTweezers software (raw data, 1s acquisition per spectrum). (d) Intensity of the prominent 1001cm^{-1} band vs. z-position from the data in (c). The red line is a fit to the data using the sum of two Gaussians.

2. HOT-RMS instrumentation and methods

2.1. Instrumentation

The initial part of the HOT-RMS instrument optical path is similar to modern HOT instruments, as seen in Fig. 1, with a NIR continuous wave laser (Ti:Sapphire tuned to 785nm, 3.9W max. power output, Spectra-physics, USA) directed through a variable attenuator, a half-wave plate (to match the laser polarization to the liquid crystal axis of the LC-SLM) and a laser-line-pass filter. Subsequently, the laser beam is expanded to slightly overfill the active area of a 512×512 pixel LC-SLM (BNS XY 512 Phase with dielectric coating, Boulder Nonlinear Systems, USA). Software-controlled phase modulation of the laser beam with the LC-SLM imprints a hologram pattern (using RedTweezer software developed by Bowman et al. [21]), such that after relaying the LC-SLM plane to the back pupil of the microscope objective using a telescope and a dichroic beamsplitter (Semrock, USA), multiple focused laser spots are generated. The LC-SLM is connected to a computer (Lenovo P500 Thinkstation with additional Asus NVIDIA GTX650 graphics card) via a DVI display cable, on which it behaves as a secondary computer monitor. Each laser focus generated in this way can be controlled independently, simultaneously functioning as an optical trap and spontaneous Raman excitation source.

The inverted microscope (Olympus IX71, Japan) with incubated enclosure (Solent Scientific,

Optics EXPRESS

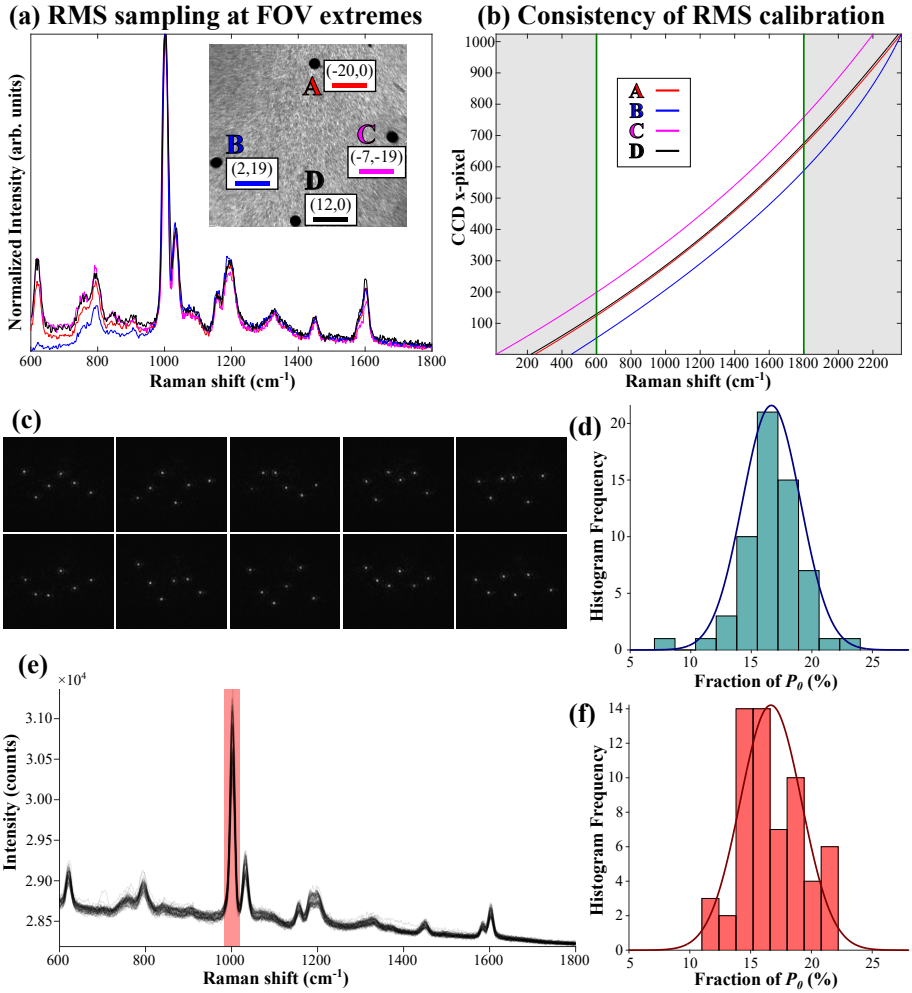

Fig. 3. HOT-RMS calibration and power consistency. (a) Four RMS spectra acquired simultaneously from bulk polystyrene at the extremes of the FOV (inset: DMD camera image co-ordinates in μm). Note: while points A and D share an overlapping co-ordinate on the CCD height axis, their spectra do not overlap as there is a slight rotation between the co-ordinate axes. (b) shows the corresponding calibration curves for each spectrum in (a) fitted to 5 bands using a 5th order polynomial. (c) Intensity variation between HOT-RMS laser spots (10 patterns, $N = 6$). Laser power was attenuated so as not to saturate the camera in order to provide a reliable intensity estimation. (d) Distribution of the 60 image-based intensity measurements as a fraction of ηP_0, with Gaussian fit (mean: 16.7% ηP_0, standard error: ±2.4% ηP_0). (e) RMS spectra corresponding to 60 measurements in (c), with corresponding distribution in (f) of area of the 1001cm^{-1} band, with Gaussian fit (mean: 16.7% ηP_0, standard error: ±2.5% ηP_0).

UK) uses a high-N.A. microscope objective (Olympus UPLSAPO 60×, 1.2 N.A., Japan) to focus the multiple laser spots at the sample through a quartz coverslip (0.17mm thick, SPS supplies) fixed to an sealed titanium chamber with a 5% CO_2 supply within the 37°C microscope enclosure (for live cell measurements). The microscope filter-cube wheel is equipped with one filter-cube containing an NIR-optimized mirror (Chroma, USA), and another containing an identical second dichroic beamsplitter to that at the microscope entrance. Both filter-cubes allow HOT capability,

Optics EXPRESS

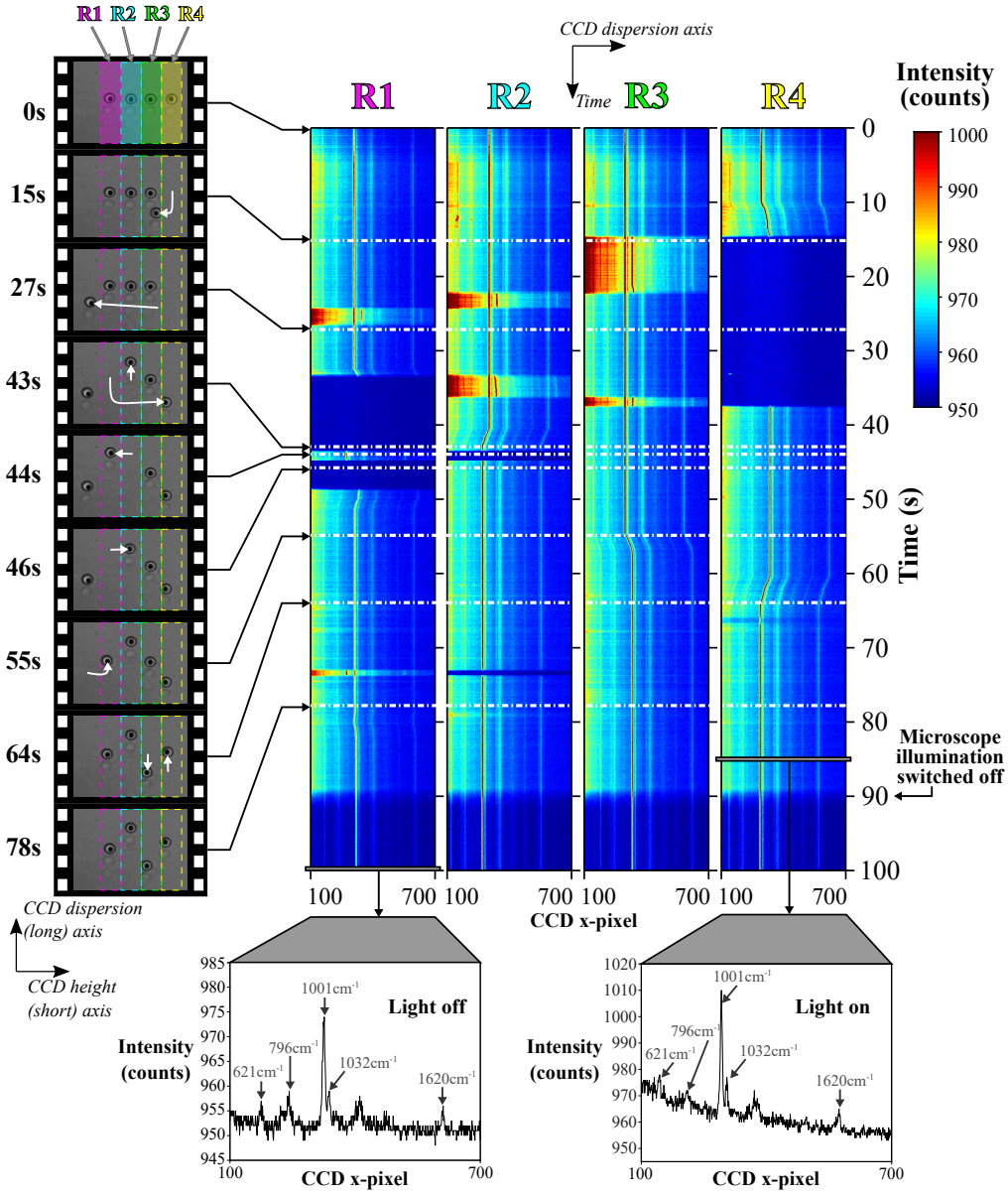

Fig. 4. Demonstration of real-time interactive optical manipulation and RMS acquisition. The numbered regions marked by colored rectangles in the movie frames (from DMD camera) correspond to four CCD binning regions used to acquire Raman spectra (see Visualization 1). These frames show manipulation of four polystyrene beads (5μm) within the different regions. During optical manipulation, binned CCD acquisitions are obtained at 10Hz (rate limited by mechanical shutter speed, exposure time 10ms indicating 100Hz readout is achievable with a faster shutter), with each readout producing four Raman spectra, one from each region. The time-resolved spectra are shown in the four colormap images (color limits adjusted for clarity). For the first 90 seconds, measurements were carried out with the microscope halogen light illumination for bright-field imaging. Co-ordinate axes labels relative to the spectrograph CCD plane are shown for the movie frames and time-course Raman spectra to aid clarity.

Optics EXPRESS

but only the NIR mirror allows combined HOT-RMS measurements. The second dichroic mirror allows conventional HOT to be carried out, with the sample also able to be imaged onto a high-speed gigabit Ethernet camera on the microscope side-port (DALSA Genie HM1024, Teledyne) after passing through a removable shortpass filter to prevent camera saturation by laser light (FES0750, Thorlabs).

For RMS measurements, backscattering is collected from each laser focus and directed out of the microscope by the NIR reflective mirror (M1 in Fig. 1). Before the Raman photons reach the spectrometer, they should ideally be spatially and spectrally filtered (the latter is carried out using a bandpass or notch filter to reject excitation wavelengths). Spatial filtering serves multiple purposes: first, any undesirable out-of-focus or stray light is rejected before entering the spectrometer (i.e. confocality is increased), and second, the spectral resolution is improved to resolve Raman linewidths with minimal spectral overlap. Typically the latter is carried out using a mechanical spectrograph entrance slit, before being dispersed within the spectrometer. Here a DMD (DLP Lightcrafter Evaluation module, Texas Instruments, USA) is instead used for spatial filtering, with reflective apertures instead of transmissive (e.g. pinhole/slit). This functions by creating a binary image in software (written as a LabVIEW plugin for the RedTweezers control software) which can be calibrated to match 1-to-1 with each laser trap co-ordinate in the sample-conjugate plane at the DMD display, which is connected by HDMI and also behaves as an additional computer monitor. A pixel is 'off' when light is directed towards an inspection imaging camera (DCC1545M CMOS, Thorlabs), and 'on' when directed through a notch filter (Semrock, USA) and into an imaging Raman spectrometer (Acton LS785, Princeton Instruments) with a fully opened 3mm mechanical entrance slit, in which a grating (1000 lines/mm, Richardson, USA) disperses the light onto a NIR-optimized 128×1024 pixel CCD detector (Andor iDus BR-DD) which is thermoelectrically cooled to -70°C.

2.2. Optimization and calibration

In order to match the DMD pinhole positions to the laser trap co-ordinates, polystyrene micro-particles were optically trapped across the usable field-of-view (FOV), and were monitored with the DMD camera and real-time Raman spectra. These readouts were used to assess the overlap between the DMD pinhole and image of the micro-particles, and the Raman signal strength respectively. Typical DMD-pinholes diameters of 110μm were found to be optimal for maintaining the high spectral resolution and optical throughput required for biological measurement, which was judged by considering the polystyrene Raman band widths compared with a standard single-beam Raman instrument. The DMD also has the added capability of choosing pinhole size in software, allowing simple optimization of the spectral resolution and confocalality trade-off vs. optical throughput, as shown in Figs. 2(a) and 2(b). The axial position of a trapped object was also optimized to maximize Raman scattering collection using LC-SLM control of axial trapping co-ordinate, as shown in Figs. 2(c) and 2(d). This resulted in an optimal focus of -9μm for polystyrene microparticles. For cells, the optimal trapping position was found to be slightly lower at around -11μm.

The power of each individual laser trap is difficult to measure directly with a power meter due to the microscopic separation of the spots at the sample. However, using the total power (P_0) of the laser spot array (readily measurable with a power meter), it is possible to estimate the laser power per trap (P_i) from P_0 according to the equation

$$P_i = \frac{\eta P_0}{N} \pm \epsilon \tag{1}$$

where η is the LC-SLM modulation efficiency, N is the total number of software-generated laser foci, and ϵ is an error term. In order to vary P_0 itself, a variable attenuator was placed before the LC-SLM allowing P_0 to span 0–800mW at the microscope objective. The η term also results in

Optics EXPRESS

a 0th order laser focus, which cannot be controlled in software, of power $(1-\eta)P_0$ fixed on the optical axis (for the LC-SLM model used here, $\eta \approx 0.9$). The error term was estimated using two approaches, the first using non-saturated microscope camera images of different laser patterns focused at a quartz-air interface (Fig. 3(c)), and the second used Raman spectra from a uniform transparent polystyrene surface (Fig. 3(c)). For the image-based measurement, the pixel values for the local region of each laser spot were integrated (measure of P_i), and summed for each group of 6 measurements (measure of ηP_0). For the Raman spectral-based approach, a similar estimation was made using the 1001cm^{-1} band area. The resulting intensity distributions from each method, shown in Figs. 3(d) and 3(f), agree well on a mean intensity fraction close to the ideal $P_i = \eta P_0/6$ (i.e. 16.7%), and suggest a relative error of P_i of approximately $\epsilon = 15\%$. Differences between these distributions are likely to be caused by intensity variations along the optical path between the sample plane and spectrograph CCD. One aspect overlooked by equation 1 is higher-order diffraction from the LC-SLM, which will result in overestimation of P_i on average. This was minimized by adjusting the look-up table (LUT) in the RedTweezers software such that higher order diffraction was minimized [21].

Raman spectral data processing

Raman spectra were processed in MATLAB (Mathworks, USA) using home-built functions. HOT-RMS spectra were acquired either by capturing the whole 128×1024 pixel CCD image for measurements where acquisition time was much longer than readout time, or using on-chip vertical binning of CCD regions to allow faster readout of multiple Raman spectra (such as in Fig. 4). For the full CCD image data, spectra were binned manually in MATLAB, with an equal number of CCD rows binned within any one acquisition to maintain consistent noise contributions.

The Raman spectra were subsequently matched to a calibrated Raman shift axis obtained from bulk polystyrene, typically using the phenyl ring breathing mode for cells. A linear shift of the calibration axis was sufficiently accurate, as test spectra from a bulk polystyrene sample at the extremes of the field of view showed minimal distortions from aberrations when these Raman spectra were calibrated, as shown in in Figs. 3(a) and 3(b). The calibrated Raman spectra were subsequently trimmed to a fixed array size, with the first element corresponding to the value closest to 600cm^{-1}, allowing combinations of different Raman spectra (e.g. mean or difference spectra). Baseline subtraction was carried out using the polynomial method by Lieber and Mahadevan-Jansen [36], and substrate signal subtraction using the method by Beier and Berger [37].

2.3. Test samples

Polystyrene beads (3μm and 5μm diameter, Sigma-Aldrich, UK) were diluted in water such that typically no more than a single microparticle was visible in the microscope field-of-view.

Pseudomonas Aeruginosa bacteria were obtained from a single colony grown on agar using a sterile loop, the bacteria from which were grown to log phase overlight in LB growth solution on a mechanical shaker, and subsequently diluted in water for HOT-RMS experiments.

Saccharomyces Cerevisiae yeast cells were diluted in pure water from dried active pellets obtained from a local supermarket (Allinson Flour, UK).

Mammalian red blood cells were obtained by centrifuging defibrinated horse blood (VWR, UK), followed by appropriate dilution in phosphate buffered saline.

2.4. Immune cell experiment methods

T cell isolation and generation of DCs were carried out as previously described [38,39]. DCs were harvested and centrifuged at 350×g for 5 minutes and suspended in RPMI® media supplemented with 10% fetal calf serum (FCS). DCs were then transferred into sample holders pre-treated with

Optics EXPRESS

10μg/ml Laminin (Sigma Aldrich, UK) and incubated for 30 minutes at 37°C with CO_2 to enable attachment. Following incubation, allogenic T cells were then added at a ratio of 1:3 DC-T cells, and time-lapse imaging was done using the microscope.

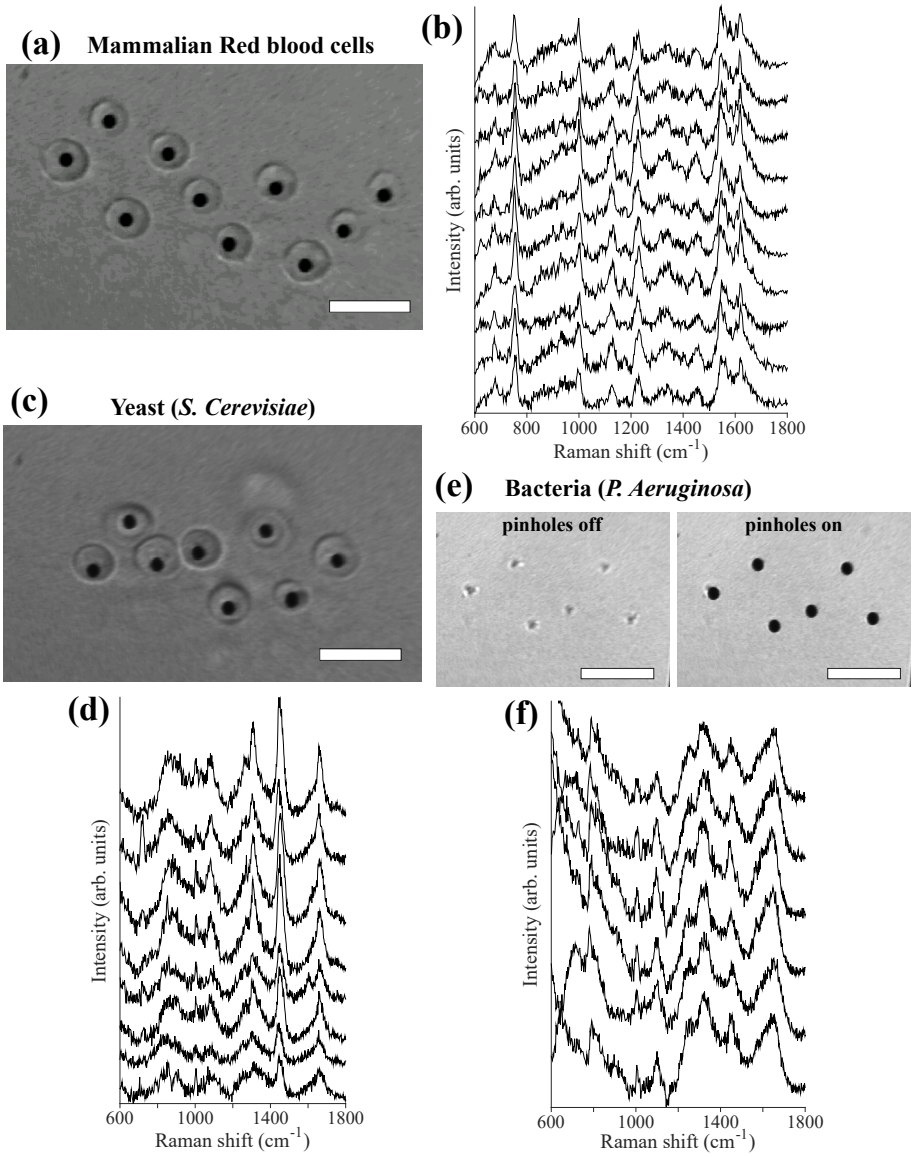

Fig. 5. Examples of HOT-RMS multi-beam trapping measurements of various cell types, with DMD camera images (scale bars 10μm) showing the fixed pinhole locations for measurement of the trapped cells (a,c,e) and Raman spectra from each trapping location (b,d,f; spectra shifted for clarity). (a,b) Mammalian red blood cells (P_i = 3mW, 60s acquisition, 5th order polynomial baseline and quartz background subtraction). (c,d) *S. Cerevisiae* yeast (P_i = 50mW, 2s acquisition, 1st order polynomial baseline subtracted). (e,f) *P. Aeruginosa* bacteria (P_i = 50mW, 10s acquisition, 1st order polynomial baseline subtraction)

Optics EXPRESS

3. Results

3.1. Dynamic HOT-RMS measurement

In order to demonstrate dynamic HOT-RMS measurement capability, Raman spectra were rapidly acquired from four trapped polystyrene spheres simultaneously, which were manipulated interactively in real-time at the sample. This was achieved using four distinct regions of the CCD, corresponding to four sample-conjugate regions. Frames from each CCD region were binned in hardware allowing independent readout at 10Hz (corresponding to 40 spectra per second), for a total time of 100s. During this time, the four trapped particles were manipulated around the four FOV regions, with microscope illumination from a halogen lamp for the first 90s. Fig. 4 shows video frames from the experiment, with the corresponding simultaneous time-course Raman spectra. Fig. 4 shows that the manipulation of a trapped particle within a particular FOV can result in a spectral shift at the detector (if a component of the displacement is along the dispersion axis of the spectrometer). A trapped particle moving between regions results in a sharp change in spectral output, with regions containing two traps resulting in overlapping spectra (i.e. cross-talk between readout from each trap). To reduce such cross-talk, the CCD regions for spectral readout can be reduced in size to match the vertical extent of the dispersed spectrum (typically 10 CCD tracks for a pinhole of 110μm). Nevertheless, this example demonstrates the capability of the HOT-RMS instrument for truly simultaneous real-time HOT-RMS measurements of multiple trapped objects, even when simulatneously recording bright-field images with halogen lamp illumination.

3.2. HOT-RMS of live cells

RMS measurements of live cells in solution typically involve using laser excitation powers around 20–200mW at the sample (at 785nm). As the spontaneous Raman effect is a relatively weak phenomenon and Raman scattering intensity scales linearly with excitation intensity, the excitation laser power would ideally be as large as possible. However above 200mW, many cells tend to be irreversibly damaged [1]. This damage threshold is not universal, and can significantly vary depending on the exact optical properties of the cells under investigation, with mammalian erythrocytes (red blood cells: RBCs) for example being much more sensitive at 785nm excitation, as they exhibit an absorption resonance leading to a damage threshold at approximately 20mW [40]. It is therefore essential to be able to control the laser power for each HOT-RMS laser trap such that excitation can be optimized whilst avoiding laser-induced damage and allowing quantitative comparison between measured Raman spectra.

Figure 5 shows examples of optically trapped cells with their correponding Raman spectra at different excitation/trapping powers. For RBCs which have a high absorption coefficient, resonant Raman spectra of hemezoin and hemoglobin are measured at 785nm excitation, enabling measurement of the multiple high SNR Raman spectra shown in Fig. 5(a) at viable laser powers as estimated by equation 1 [40]. For similarly sized cells such as yeast, excitation is possible at larger P_i, so Raman spectra of similar SNR can be obtained with shorter acquisition times, as shown in Fig. 3(b). It is also possible to measure smaller trapped cells such as bacteria at similar P_i to yeast as seen in Fig. 5(c), though the integration time required is typically longer as bacteria have lower total biomass which will undergo Raman scattering within the laser focus.

Laser-damage mechanisms possible during RMS measurements may involve two-photon absorption, laser-induced heating, and photochemical reactions of particular light-sensitive compounds (e.g. porphyrins) within cells [1]. For RMS at 785nm excitation, it is often the latter effect responsible for damage. In some cases, time-course Raman spectra of trapped cells may show spectral changes which indicate the mechanism of laser-induced damage. RBCs are one such case, as the resonant Raman signal of the hemoglobin provides sufficient SNR and specificity to monitor the laser-induced aggregation with a reasonable temporal resolution. Fig. 6(a) shows

Optics EXPRESS

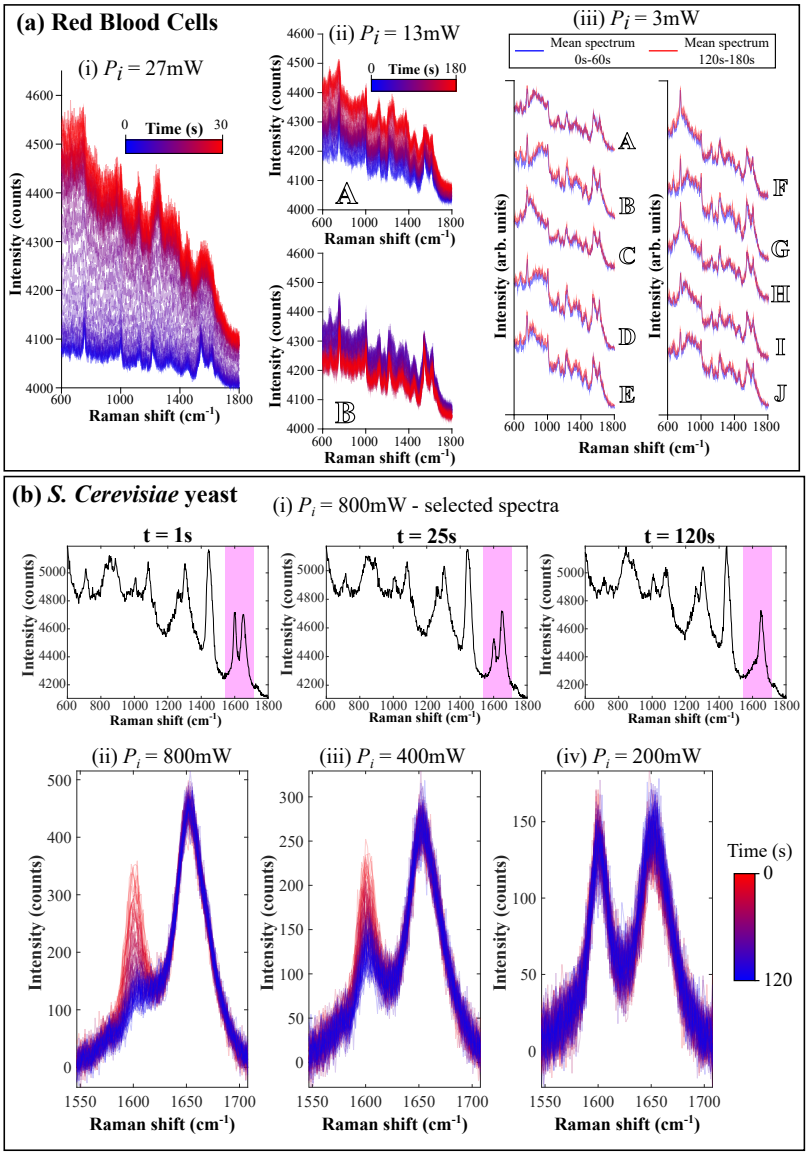

Fig. 6. Control of laser power for HOT-RMS measurements. (a): Time-course Raman spectra (raw data) of red blood cells (RBCs) trapped at various laser power P_i. (i) Rapid changes in the Raman spectra of a RBC trapped at P_i = 27mW can be seen (0.5s per spectrum). (ii) Two RBCs trapped with P_i = 13mW also show some change over time, though at a reduced rate (2.5s acquisition per spectrum). (iii) Ten RBCs trapped with P_i = 3mW, with the mean of the first and last 60s of a 180s time-course Raman spectra acquisition shown. (b): Time-course Raman spectra of *S. Cerevisiae* yeast trapped at various laser power P_i. (i) Raman spectra from selected time-points of a time-course measurement of a yeast cell trapped with P_i = 800mW (raw data). Time-course baseline-subtracted Raman spectra of trapped yeast, focusing on the 1550–1700cm^{-1} region are shown for (ii) P_i = 800mW, (iii) P_i = 400mW, and (iv) P_i = 200mW.

Optics EXPRESS

RBCs used as a test case, whereby cells trapped with different values of P_i, ranging from 3mW to 27mW, with time-course Raman spectra acquired starting from the moment the cells are captured in a trap. Fig. 6(a)(i) shows that with P_i = 27mW (above the damage threshold [40]), the time-course spectra show a rapid spectral change over the course of 30s. The differences show an increase in baseline indicating increased fluorescence, as well as a change in certain Raman band intensities, particularly the 1250cm^{-1} band, which has previously been assigned as a denaturation and aggregation biomarker [40].

Figure 6(a)(ii) shows a similar measurement with two cells trapped and measured simultaneously, with P_i = 13mW which is below the estimated laser damage threshold. The time-course Raman spectra over 180s show that cell A experiences similar denaturation and aggregation to that in Fig. 6(a)(i), albeit at a reduced rate. In contrast, the Raman spectra from cell B shows minimal change, with a slight decrease in signal. The difference between these two cells measured at the same expected value of P_i could be due to the error ϵ mentioned in equation 1 leading to one beam being above the damage threshold with the other below the threshold, or possibly from inter-cellular differences such as the cell size or a different concentration of hemoglobin within the cell.

Figure 6(a)(iii) shows a measurement with P_i = 3mW for ten simultaneously trapped RBCs. The spectra shown are averages of the first and last 60s of the time-course Raman spectra (over 180s total), which show no measurable differences above the noise level of the measurement, suggesting immediate laser-induced damage has been avoided for all ten cells in the trap.

A second example is demonstrated for individual trapped yeast cells (*S. Cerevisiae*) in Fig. 6(b), which have a convenient Raman band biomarker at 1602cm^{-1}, the so-called "signature of life" [5]. The origin of this Raman band is thought to be due to the presence of ergosterol [41], a functional equivalent to cholesterol within fungal cells, which has a conjugated C=C bond assigned to 1602cm^{-1}. The presence of ergosterol has been linked to cell metabolism, with chemical- and laser- induced cell-death previously observed.

Figure 6(b)(i) shows snapshot Raman spectra from a time-series acquisition of a single yeast cell trapped and measured using maximum available laser power, with the 1602cm^{-1} band decreasing with laser exposure time as seen in the close-up in Fig. 6(b)(ii). Measurement at a reduced laser power of 400mW in Fig. 6(a)(iii) suggests the 1602cm^{-1} band still decreases over time, but at a reduced rate compared to the measurement at 800mW. Fig. 6(a)(iv) shows no change was observed for 200mW trapping/excitation power over the measurement time of 120s.

The measurements in Fig. 6 demonstrate that P_i can be sufficiently controlled to optimize measurements for cells on a case-by-case basis, and that optical throughput is sufficient using DMD-based spatial filtering for Raman spectroscopy. While not all cells will exhibit such distinct spectral markers for laser damage as RBCs and yeast, other metrics such as baseline change in raw data could potentially be used for assessing laser damage.

These results also suggest that using a higher excitation power for a shorter measurement/trapping time may be feasible with sufficiently high-throughput Raman detection (i.e. a Raman spectrum can be measured before lasting damage is done), which may be practically useful for applications such as Raman activated cell sorting.

3.3. HOT-RMS for inducing and measuring immunological synapses

To demonstrate the capability of the HOT-RMS instrument for cell biology applications, we manipulated multiple live T cells, bringing them controllably into contact with a dendritic cell (DC) to initiate the formation of an immunological synapse (IS) junction, and measuring space- and time- resolved Raman spectra.

Figure 7 shows an example of an induced interaction between multiple T cells and DCs using HOT with measurement at different locations and time points using RMS. All HOT and RMS measurements were acquired with 6 active traps at any one time (P_i = 50mW), and the laser

Optics EXPRESS

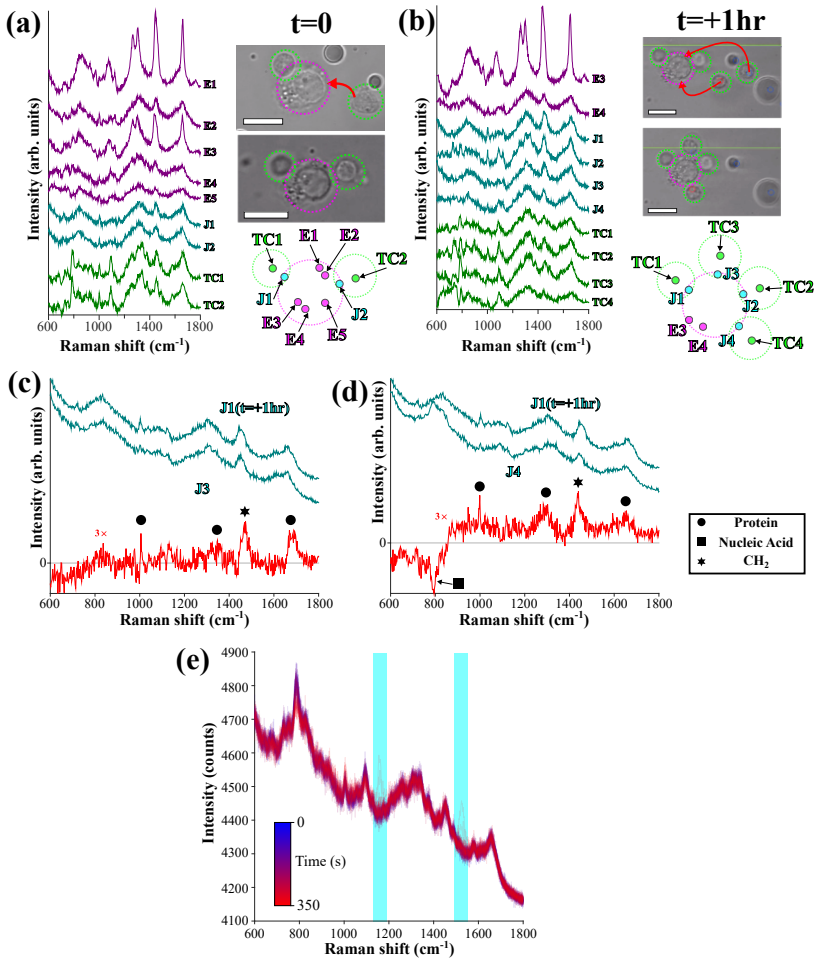

Fig. 7. Formation of an immunological synapse (IS) between an adherent dendritic cell (DC) and optically trapped T cells monitored by RMS. (a) Raman spectra and microscope images at t=0 when a DC with one T cell already interacting has another T cell brought into contact using the HOT-RMS instrument. The schematic shows the locations from which Raman spectra were acquired (20s acquisition). (b) Raman spectra and microscope images showing further induced interactions with two more trapped T cells brought into contact with the same DC in (a) at t=+1hr, with a second schematic showing estimated sampling locations. (c) and (d) show Raman difference spectra between the oldest IS junction (J1) and the new junctions J3 and J4 (measured at t=+1hr shortly after their formation). Raman spectra in (a) and (b) have a linear baseline and quartz background subtracted, wheras (c) and (d) show raw Raman spectral data. (e) Time-course Raman spectra for a trapped T cell (raw data), with carotenoid Raman band locations at 1157cm^{-1} and 1525cm^{-1} highlighted. All scale bars 10μm.

was blocked from the sample between trapping/Raman acquisitions. A time-course Raman acquisition for a trapped T cell in these conditions is shown in Fig. 7(e), with no significant changes observed other than the occasional presence of carotenoid Raman bands, possibly from the movement of a cytoplasmic granule in/out of the measurement volume [42]. The example interaction shown in Fig. 7 involves a DC with an existing connection to a T cell (labelled TC1). The microscope image shown in Fig. 7 (a) shows the process of initiating a second interaction

Optics EXPRESS

between the DC and an optically trapped T cell (TC2) at time t=0. Attachment was verified by attempting to trap and pull off the T cells after waiting for a short time. A cell was considered attached once the laser trap was incapable of moving the T cell. Once TC2 was attached, Raman spectra from various points were acquired over the course of 5 minutes, with selected spectra shown from the labelled positions in the schematic in Fig. 7(a), focusing particularly on T cells (green), DC edges (purple) and junctions (blue). It can be seen that the T cell spectra (TC1 and TC2) contain relatively strong Raman contributions from nucleic acids (788cm^{-1} and 1090cm^{-1}) and proteins (1004cm^{-1} and 1660cm^{-1}), in agreement with previous studies [9, 10]. In contrast, DCs generally have a weaker Raman signal which varies spatially, with certain regions showing lipid droplet signals (E1,E3).

Figure 7(b) shows the interacting system after t=+1hr, when two additional T cells were trapped and brought towards the DC for a further interaction. After this, several Raman spectra were obtained in a similar manner to Fig. 7(a) at the locations shown in the schematic in Fig. 7(b). Similar observations can be made to the measurements shortly after t=0, with the exception of the newly formed junctions, J3 and J4, between the DC and the T cells TC3 and TC4.

The Raman spectra from the various locations shown in Figs. 7(a) and 7(b) can be compared to identify dynamic changes occuring in the interacting cell system. The Raman bands from the T cells and DC edges appear to be consistent at both timepoints. However the differences between the Raman spectra measured at the junctions suggest molecular differences, in particular protein content. Figs. 7(c) and 7(d) show the Raman difference spectra between J1 (the earliest junction formed between a T cell and the DC, as measured at t=0) and J3 and J4 respectively induced by HOT at time t=+1hr. The difference appears to mainly contain Raman bands assigned to proteins, particularly the prominent 1004cm^{-1} band (breathing mode of phenylalanine ring) which appears larger relative to the 1450cm^{-1} (CH_2 and CH_3 deformation vibrations) in the difference spectrum compared to the individual Raman spectra, suggesting the junctions which formed earliest have a larger protein content. Previous studies of fixed DCs and T cells comparing Raman spectral imaging and fluorescence staining of actin indicated that such changes in protein level may be linked to actin polarisation at the IS [10]. These differences may also be due to an increased measurement volume between the sampling locations, and would require thickness/morphology measurement to conclusively determine which case these measurements fall into [14].

This demonstration of a HOT-RMS measurement between multiple dynamically interacting cells demonstrates the capability of the instrument for label-free molecular sensing. As optical trapping can be used for T cell manipulation, interactions between the immune cells can be monitored from the start, with endogenous molecular changes at the formed junctions detected by RMS. Such capability could offer previously unattainable insight into the kinetics of biochemical changes during all time-points of cell-cell interactions.

4. Conclusion

We have demonstrated that HOT-RMS is a promising tool for simultaneous non-invasive manipulation and RMS molecular measurement of interacting living organisms. Raman spectra with spectral resolution from diffraction limited points were able to be obtained from multiple trapped objects simultaneously in arbitrary locations in the field of view, with high temporal resolution. We have demonstrated the general applicability of such an instrument, measuring bacteria, yeast, blood and mammalian immune cells. The capability for high-resolution time-course RMS spectra and accurate laser trap power control can also be used to assess laser-induced damage thresholds and measurement viability.

Funding

Engineering and Physical Sciences Research Council (EPSRC) (EP/L025620/1, EP/M506588/1).

Optics EXPRESS

Acknowledgments

The authors would like to thank Professor Paul Williams and Dr. James Brown for providing samples of planktonic *P. Aeruginosa* bacteria for HOT-RMS measurements. This work was supported by the Engineering and Physical Sciences Research Council [grant number EP/L025620/1, EP/M506588/1].

Disclosures

The authors declare that there are no conflicts of interest related to this article.

References

1. D. W. Shipp, F. Sinjab, and I. Notingher, "Raman spectroscopy: Techniques and applications in the life sciences," Adv. Opt. Photonics **9**, 315–428 (2017).
2. B. Kann, H. L. Offerhaus, M. Windbergs, and C. Otto, "Raman microscopy for cellular investigations-from single cell imaging to drug carrier uptake visualization," Adv. Drug Deliv. Rev. **89**, 71–90 (2015).
3. K. Maquelin, C. Kirschner, L.-P. Choo-Smith, N. van den Braak, H. P. Endtz, D. Naumann, and G. Puppels, "Identification of medically relevant microorganisms by vibrational spectroscopy," J. Microbiol. Methods **51**, 255–271 (2002).
4. J. W. Chan, A. Esposito, C. Talley, C. Hollars, S. Lane, and T. Huser, "Reagentless identification of single bacterial spores in aqueous solution by confocal laser tweezers Raman spectroscopy," Anal. Chem. **76**, 599–603 (2004).
5. Y.-S. Huang, T. Karashima, M. Yamamoto, T. Ogura, and H.-o. Hamaguchi, "Raman spectroscopic signature of life in a living yeast cell," J. Raman Spectrosc. **35**, 525–526 (2004).
6. G. Puppels, F. Demul, C. Otto, J. Greve, M. Robertnicoud, D. Arndt-Jovin, and T. Jovin, "Studying single living cells and chromosomes by confocal Raman spectroscopy," Nature **347**, 301–303 (1990).
7. A. Ghita, F. C. Pascut, V. Sottile, and I. Notingher, "Monitoring the mineralisation of bone nodules in vitro by space-and time-resolved Raman micro-spectroscopy," Analyst **139**, 55–58 (2014).
8. M. Okada, N. I. Smith, A. F. Palonpon, H. Endo, S. Kawata, M. Sodeoka, and K. Fujita, "Label-free Raman observation of cytochrome c dynamics during apoptosis," Proc. Natl. Acad. Sci. **109**, 28–32 (2012).
9. M. D. Mannie, T. J. McConnell, C. Xie, and Y.-Q. Li, "Activation-dependent phases of T cells distinguished by use of optical tweezers and near infrared Raman spectroscopy," J. Immunol. Methods **297**, 53–60 (2005).
10. A. B. Zoladek, R. K. Johal, S. Garcia-Nieto, F. Pascut, K. M. Shakesheff, A. M. Ghaemmaghami, and I. Notingher, "Label-free molecular imaging of immunological synapses between dendritic and T cells by Raman micro-spectroscopy," Analyst **135**, 3205–3212 (2010).
11. A. Naemat, H. M. Elsheikha, R. A. Boitor, and I. Notingher, "Tracing amino acid exchange during host-pathogen interaction by combined stable-isotope time-resolved Raman spectral imaging," Sci. Reports **6**, 20811 (2016).
12. A. Naemat, F. Sinjab, A. McDonald, A. Downes, A. Elfick, H. M. Elsheikha, and I. Notingher, "Visualizing the interaction of acanthamoeba castellanii with human retinal epithelial cells by spontaneous raman and CARS imaging," J. Raman Spectrosc. **49**, 412–423 (2018).
13. I. Notingher, I. Bisson, A. E. Bishop, W. L. Randle, J. M. Polak, and L. L. Hench, "In situ spectral monitoring of mRNA translation in embryonic stem cells during differentiation in vitro," Anal. Chem. **76**, 3185–3193 (2004).
14. R. Boitor, F. Sinjab, S. Strohbuecker, V. Sottile, and I. Notingher, "Towards quantitative molecular mapping of cells by Raman microscopy: using AFM for decoupling molecular concentration and cell topography," Faraday Discuss. **187**, 199–212 (2016).
15. J. W. Chan, D. S. Taylor, T. Zwerdling, S. M. Lane, K. Ihara, and T. Huser, "Micro-Raman spectroscopy detects individual neoplastic and normal hematopoietic cells," Biophys. J. **90**, 648–656 (2006).
16. J. W. Chan, D. S. Taylor, S. M. Lane, T. Zwerdling, J. Tuscano, and T. Huser, "Nondestructive identification of individual leukemia cells by laser trapping Raman spectroscopy," Anal. Chem. **80**, 2180–2187 (2008).
17. A. Ashkin, J. M. Dziedzic, J. Bjorkholm, and S. Chu, "Observation of a single-beam gradient force optical trap for dielectric particles," Opt. Lett. **11**, 288–290 (1986).
18. A. Ashkin, J. M. Dziedzic, and T. Yamane, "Optical trapping and manipulation of single cells using infrared laser beams," Nature **330**, 769–771 (1987).
19. D. G. Grier, "A revolution in optical manipulation," Nature **424**, 810–816 (2003).
20. R. W. Bowman and M. J. Padgett, "Optical trapping and binding," Reports on Prog. Phys. **76**, 026401 (2013).
21. R. W. Bowman, G. M. Gibson, A. Linnenberger, D. B. Phillips, J. A. Grieve, D. M. Carberry, S. Serati, M. J. Miles, and M. J. Padgett, ""Red Tweezers": Fast, customisable hologram generation for optical tweezers," Comput. Phys. Commun. **185**, 268–273 (2014).
22. C. Xie, M. A. Dinno, and Y.-Q. Li, "Near-infrared Raman spectroscopy of single optically trapped biological cells," Opt. Lett. **27**, 249–251 (2002).
23. R. Gessner, C. Winter, P. Rösch, M. Schmitt, R. Petry, W. Kiefer, M. Lankers, and J. Popp, "Identification of biotic and abiotic particles by using a combination of optical tweezers and in situ Raman spectroscopy," ChemPhysChem **5**, 1159–1170 (2004).

Optics EXPRESS

24. C. Xie, C. Goodman, M. A. Dinno, and Y.-Q. Li, "Real-time Raman spectroscopy of optically trapped living cells and organelles," Opt. Express **12**, 6208–6214 (2004).
25. C. Xie, D. Chen, and Y.-q. Li, "Raman sorting and identification of single living micro-organisms with optical tweezers," Opt. Lett. **30**, 1800–1802 (2005).
26. A. Y. Lau, L. P. Lee, and J. W. Chan, "An integrated optofluidic platform for Raman-activated cell sorting," Lab on a Chip **8**, 1116–1120 (2008).
27. R. D. Snook, T. J. Harvey, E. C. Faria, and P. Gardner, "Raman tweezers and their application to the study of singly trapped eukaryotic cells," Integr. Biol. **1**, 43–52 (2009).
28. P. Zhang, L. Kong, P. Setlow, and Y.-Q. Li, "Multiple-trap laser tweezers Raman spectroscopy for simultaneous monitoring of the biological dynamics of multiple individual cells," Opt. Lett. **35**, 3321–3323 (2010).
29. L. Kong, P. Zhang, G. Wang, J. Yu, P. Setlow, and Y.-q. Li, "Characterization of bacterial spore germination using phase-contrast and fluorescence microscopy, Raman spectroscopy and optical tweezers," Nat. Protoc. **6**, 625–639 (2011).
30. J. W. Chan, "Recent advances in laser tweezers Raman spectroscopy (LTRS) for label-free analysis of single cells," J. Biophotonics **6**, 36–48 (2013).
31. L. Kong and J. Chan, "A rapidly modulated multifocal detection scheme for parallel acquisition of Raman spectra from a 2-D focal array," Anal. Chem. **86**, 6604–6609 (2014).
32. J. Qi and W.-C. Shih, "Parallel Raman microspectroscopy using programmable multipoint illumination," Opt. Lett. **37**, 1289–1291 (2012).
33. P. Verveer, Q. Hanley, P. Verbeek, L. Van Vliet, and W. Jovin, "Theory of confocal fluorescence imaging in the programmable array microscope (PAM)," J. Microsc. **189**, 192–198 (1998).
34. G. Gibson, M. Dienerowitz, P. Kelleher, A. Harvey, and M. Padgett, "A multi-object spectral imaging instrument," J. Opt. **15**, 085302 (2013).
35. F. Sinjab, K. Kong, G. Gibson, S. Varma, H. Williams, M. Padgett, and I. Notingher, "Tissue diagnosis using power-sharing multifocal Raman micro-spectroscopy and auto-fluorescence imaging," Biomed. Opt. Express **7**, 2993–3006 (2016).
36. C. A. Lieber and A. Mahadevan-Jansen, "Automated method for subtraction of fluorescence from biological Raman spectra," Appl. Spectrosc. **57**, 1363–1367 (2003).
37. B. D. Beier and A. J. Berger, "Method for automated background subtraction from Raman spectra containing known contaminants," Analyst **134**, 1198–1202 (2009).
38. F. Salazar, L. Hall, O. H. Negm, D. Awuah, P. J. Tighe, F. Shakib, and A. M. Ghaemmaghami, "The mannose receptor negatively modulates the toll-like receptor 4–aryl hydrocarbon receptor–indoleamine 2, 3-dioxygenase axis in dendritic cells affecting t helper cell polarization," J. Allergy Clin. Immunol. **137**, 1841–1851 (2016).
39. S. García-Nieto, R. K. Johal, K. M. Shakesheff, M. Emara, P.-J. Royer, D. Y. Chau, F. Shakib, and A. M. Ghaemmaghami, "Laminin and fibronectin treatment leads to generation of dendritic cells with superior endocytic capacity," PLoS one **5**, e10123 (2010).
40. B. R. Wood, P. Caspers, G. J. Puppels, S. Pandiancherri, and D. McNaughton, "Resonance Raman spectroscopy of red blood cells using near-infrared laser excitation," Anal. Bioanal. Chem. **387**, 1691–1703 (2007).
41. L.-D. Chiu, F. Hullin-Matsuda, T. Kobayashi, H. Torii, and H.-o. Hamaguchi, "On the origin of the 1602 cm–1 Raman band of yeasts; contribution of ergosterol," J. Biophotonics **5**, 724–728 (2012).
42. G. Puppels, H. Garritsen, J. Kummer, and J. Greve, "Carotenoids located in human lymphocyte subpopulations and natural killer cells by Raman microspectroscopy," Cytom. Part A **14**, 251–256 (1993).